Applied GIS

a free, international, refereed e-journal
(ISSN: 1832-5505)

URL:
http://www.appliedgis.net

MANAGING EDITOR:
Ray Wyatt – ray.wyatt@unimelb.edu.au

Volume 13, Number 2
November, 2017

CONTENTS:

All papers published during 2017 are part of *Volume* 13.
Each paper constitutes one *Number.*

Hence this paper should be cited as:
Sreedhar, M., Narender, B. & Muralikrishnan, S. (2017) – Line of sight analysis for urban
mobile applications: a photogrammetric approach, *Applied GIS*, 13(2), 1-19

Line of sight analysis for urban mobile applications:
a photogrammetric approach

M. Sreedhar

Aerial Services and Digital Mapping Area,
National Remote Sensing Centre,
Hyderabad, India
Sreedhar_m@nrsc.gov.in

B. Narender

Aerial Services and Digital Mapping Area,
National Remote Sensing Centre,
Hyderabad, India

S. Muralikrishnan

Aerial Services and Digital Mapping Area,
National Remote Sensing Centre,
Hyderabad, India

Abstract–Although inter visibility analysis between a GPS receiver and visible satellites is crucial for any real-time route navigation, traditional, mission-planning software does not incorporate it – they simply assume that the earth is flat. This paper seeks to correct the situation by outlining an advanced, semi-global matching technique which derives a Digital Surface Model (DSM), depicting the topography model of the earth surface for any study area. Our approach uses a GIS, combined with a freely available Global Navigation Satellite System (GNSS), to accurately predict pseudo satellite locations before building three-dimensional models of buildings from their footprints. We exploit high-resolution satellite data (*Cartosat-1* and *Geoeye-1*) along with high-density elevation information, and we ultimately reduce the need for full-scale surveys and so minimize costs and time. Moreover, our combining of 3D models with GPS-derived, ephemeris data pertaining to densely built-up areas constitutes a valuable input for real time, mobile applications like car navigation systems, personal navigation, fleet tracking, asset tracking and general, location-based services.

Keywords - *Cartosat-1*; *Geoeye-1*, DSM, Line of sight, GAGAN, IRNSS, mobile applications.

1. Introduction

Current mission-planning software packages for Global Positioning Systems (GPS) regard the earth as a flat surface. They also assume that there are no obstructions on the horizon, although some are now capable of modelling simple obstructions whereby portions of the visible horizon can be blocked out. Such an approach seriously constrains software applicability in many survey situations. Particularly when topographic surveys are carried out

within densely built-up areas. In these circumstances, obstruction of satellite signals is almost certain to be present.

Hence there is a need to enhance the prediction capabilities of Global Navigation Satellite System(GNSS) by having them note potential obstructions derived from high-resolution, digital surface models and by recording building footprints prior to survey in order to minimize GNSS outages. Accordingly, this paper will use a basic line of sight analysis to identify any obstruction that blocks the sight vector between any viewpoint and the target (Guth, 2004).

Digital Surface Models (DSMs) are often used for inter visibility analysis between a GPS receiver and GPS satellites to enable real-time, route navigation. While new techniques such as LIDAR are available for almost instant digital surface model generation, stereoscopic, high-resolution satellite imagery coupled with image matching affords a more cost-effective plotting of surface topography over large-coverage areas. As such, such a combination is a viable alternative to aerial photographs (Poon et al, 2005). Optical, very high-resolution (VHR) satellites have frequently generated accurate cartographic products, such as orthoimages and digital surface models (Toutin, 2004).

Most of the high-resolution satellite sensors, for example *Cartosat-1, ALOS-PRISM, Formosat-2, Ikonos, QuickBird, Geoeye-1*and *WorldView-1*have an along-track solution (Toutin, 2004) and this produces consistent imaging conditions and so increases the image-matching success rate (Poon et. al., 2005). The *Cartosat-1* satellite for instance, launched in May 2005 by ISRO, is an along track stereo (aft −5, fore +26°) with 2.5m GSD. and it gives a base-height ratio of 0.63 with a 27km swath (Muralikrishnan et al., 2012). Data from this satellite has been extensively used because of its stereo applications and accuracy.

Indeed, the ISPRS ISRO Cartosat-1 Scientific Assessment Programme (CSAP) undertook 14 investigations around the world with local data (11 sites) and carried out evaluations of performance and the accuracy of the digital surface model and the orthoimage. Results showed that a digital surface model can be generated with an accuracy of 0.5 pixels in planimetry and 1–2 pixels (1σ) in height (Nandakumar et al.,2008).

Also, the *GeoEye-1* (*GE1*) satellite, launched in 2008, is a commercial, very high-resolution satellite with geometric resolution for both PAN and multispectral (MS) products, with nominal GSD at nadir of 0.41m and 1.65 m. All the image products from *GE1* have to be down-sampled in 0.5m and 2 m in PAN and MS. Data from*Geoeye-1* has been extensively assessed for stereo satellite elevation accuracy, and results show that vertical accuracies have a 0.25m standard deviation (Mitchell et al., 2010) and a root mean square error of 0.25m (Fraser et al., 2009).

Various image-matching techniques are available for generating digital surface models from stereo-satellite data, and each has its own merits. Therefore, when selecting one to use, various factors need to be considered, such as accuracy, handling of radiometric differences, ability to match low textured areas while preserving edges and sharp object boundaries, capability of resolving fine spatial structures on the object surface and independence of task-dependent parameter settings. Comprehensive reviews of stereo matching techniques are given by Scharstein et al. (2002), Hirschmüller et al. (2007) and Deepika Kumara & Kamaljit Kaur (2016).

Stereo-related algorithms are generally categorised into two main classes: local and global. The local or the window-based approach trades accuracy for speed and is sensitive to occluded regions (Nalpantidis, et al., 2007). By contrast, global methods are precise but time consuming and they often fail to scale with image size (Hirschmüller et al.,2007). However, many of these drawbacks can be addressed by using semi-global matching that successfully combines concepts of global and local stereo methods for accurate, dense, pixel-wise matching with low runtime (Hirschmüller, et al.,2008).

In the recent years, using remotely sensed images for automatic building extraction and reconstructing of their full, three-dimensional (3D) form has been an important topic of research. But building reconstruction from high-resolution satellite images (HRSI) in pan (panchromatic) image is a complicated problem, due to extensive spectral variations within building and non-building features (Mohsen, Ghania et al., 2016).

Most methods for building boundary extraction and 3D model reconstruction are either model-driven and data-driven. Model-driven strategies generate optimal simulations of roofs by fitting predefined, parameterized roof models to point clouds of buildings and minimizing a cost function (Partovi et al., 2015). By contrast, data-driven strategies, such as region growing, hough transform and RANSAC, extract roof planes and other geometrical information of buildings from their point clouds or dense meshes - roof planes are extracted by determining the vertices, ridge lines, and eaves (Sohn et al., 2008).

Although automatic approaches are robust and perform well in most situations, developing an operational, fully automated procedure which is generally applicable to surface reconstruction from large-scale (aerial and satellite) imagery over dense urban areas remains an unsolved problem despite many efforts in the photogrammetric and computer vision disciplines (Zhang, 2005). Cities are made up of a dense and complex mixture of artificial and natural urban features, and they vary immensely in size, shape, composition and arrangement (Mesev, 2003). Such diversity often hampers automation processes.

Note that Sreedhar et al. (2015) achieved automatic filtering and classification of a digital surface model using multi-date, stereo data from *Cartosat-1*to locate bare earth. Their technique classified ground and non-ground points, which can be indirectly used to derive building height information whenever existing building footprints are present.

Also, there are various classification techniques based upon least square's interpolation for removing off-terrain points from dense point information that has been generated from Lidar and aerial data (Sithole et al., 2004). Such methods include erosion/dilation functions in mathematical morphology (Zhang et al.,2003), slope based functions (Sithole et al.,2004), TIN densification (Axelsson, 2000) and spline functions (Briese et al.,2001), although little research has been carried out on how to automatically filter off-terrain points, like buildings, from high-resolution satellite data.

All the above filters have their own merits, and so when selecting one it is necessary to consider factors such as the distribution of features over the terrain, the performance of filtering algorithms whenever point density varies and the filter's ability to handle surfaces with discontinuities. Nevertheless, TIN densification seems to have a distinct advantage because it can handle surfaces with discontinuities. This is a particularly useful attribute if one is working in urban areas.

The important civilian-oriented, GPS tasks of fleet management, vehicle navigation and asset tracking require continuity, reliability and accuracy for providing positioning information, and this is why currently available GNSS receivers are capable of mitigating multipath signals. If they were receiving reflected signals within dense urban areas it would result in substantial positioning errors (Groves et al., 2012).

Note that to get a 3D positional fix (Grewal et al., 2007), at least four satellites are required, and if in Real-Time Kinematic (RTK) mode at least five satellites are needed. If an adequate number of satellites is not visible, the desired results will not be achieved, which will boost project cost due to the need for resurveying. Fortunately, however, prediction of satellite availability at any location within an unobstructed area is relatively easy to obtain through free, GNSS prediction software such as *Trimble Planning* (Trimble Planning, 2015) or similar online tools.

In the earlier studies, local obstructions were modelled by simply adding to each building's footprint-derived rooftop with low-density, elevation data that did not actually exist (Cahalane, 2015). Moreover, some of these studies used surface models generated directly

from raw LiDAR points. A frequent outcome was false representation of buildings, with sloping walls and erroneous triangles which in no way reproduced the true shape of the roof. Subsequent integration with aerial photogrammetry techniques was, therefore, required for accurate line of sight studies (George, Taylor et al.,2007).

Almost no research has used high-density, elevation data to extend footprints derived from high-resolution, satellite data and so achieve accurate, line of sight models of densely built-up areas. Consequently, this paper aims to do just that. It will use building footprints captured from two different high-resolution satellite data sets, and it will use GIS to combine existing, freely available Global Navigation Satellite System (GNSS) prediction software to accurately predict pseudo satellite locations. It will then access three-dimensional models derived from orthoimages and high density, elevation data, which should reduce the need for a full ground survey and so minimize time and cost. The 3D buildings thus derived will enhance the performance of visualization and line of sight analyses within mobile applications.

2. Study area and data sources

Our study area covers part of Hyderabad city, capital of Telangana state, in India. It is located between latitudes of 17°24'53'' and 17°31'24'' north, and longitudes of 78°20'39" and 78°26'58" east, with elevation ranging from 446m to 665m with respect to the WGS84 ellipsoid. Five data sets were used in this study. These were the stereo data acquired from the *Cartosat-1* and *Geoeye-1* satellite sensors, high-density elevation data derived from DSM, building footprints captured from orthoimages, GNSS almanacs in the *Trimble Planning* software and manual stereo measurements of building heights. Building heights were validated using manual, stereo measurements acquired at two different point of time – 2005 and 2012, and the parameters of the stereo data are given in Table 1.

Sensor	Acquisition Month	Nominal collection Azimuth (degrees)	Sun Elevation (degrees)
Cartosat-1	Jun-2005	191.727	69.49
Geoeye-1	Oct-2012	186.470	77.58

Table 1 – The stereo data's acquisition parameters

3. Methodology

The study had four distinct stages:

1. photogrammetric processing of stereo data by block triangulation, with a sub-process involving digital surface model generation, orthophoto production and manual vectorization of building footprints,
2. filtering the digital surface model,
3. building height extraction, and
4. application of line of sight functions in GIS to ascertain visibility using the GPS satellites.

3.1. Photogrammetric processing of stereo data

The flowchart for this stage is shown in Figure 1. Whereas *Cartosat-1*'s stereo ortho-kit provided image data and associated rational polynomial coefficient (RPCs) files for both the aft and fore images, *Geoeye-1*gave stereo data in the form of a geo-stereo product. The RPCs facilitated a direct mapping, from 3D object coordinates that were usually offset by normalized latitude, longitude and height to 2D image coordinates (usually offset by normalized line and sample values). Note that RPCs are generally the ratio of two polynomials that use parameters derived from the rigorous sensor model's approximate
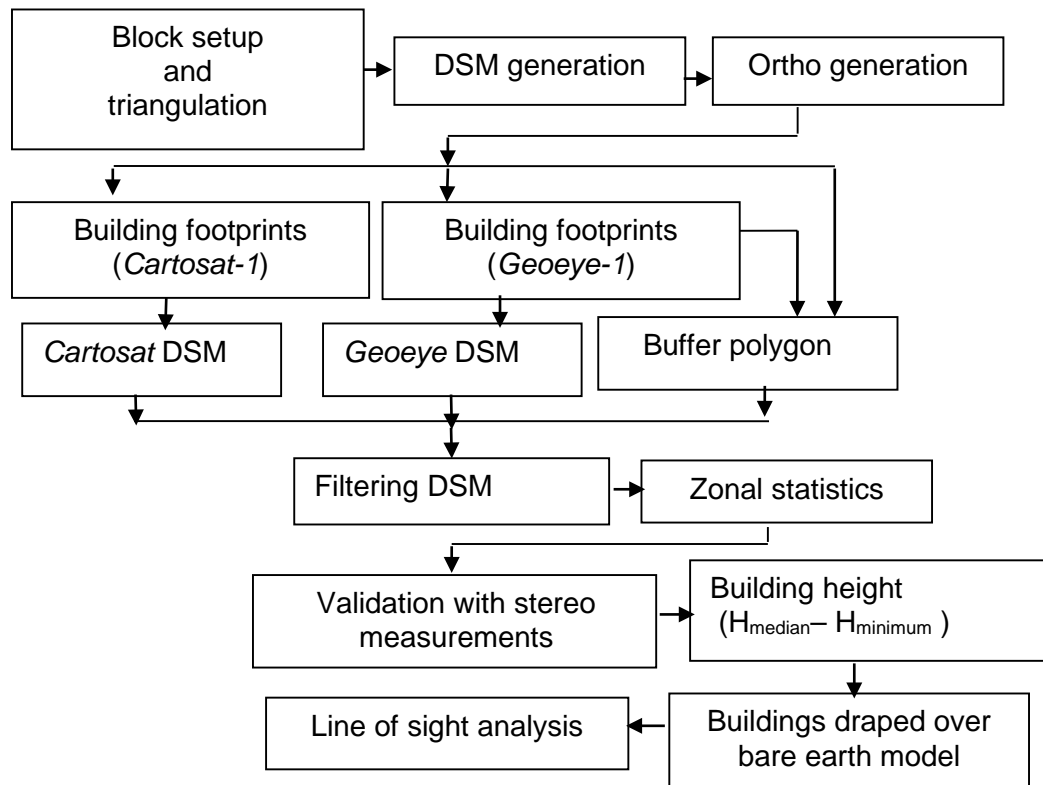
orientation (Grodecki et al., 2003).

```
┌─────────────┐      ┌──────────────┐      ┌──────────────┐
│ Block setup │ ───► │     DSM      │ ───► │    Ortho     │
│    and      │      │  generation  │      │  generation  │
│triangulation│      └──────────────┘      └──────────────┘
└─────────────┘
```

Figure workflow:

- Block setup and triangulation → DSM generation → Ortho generation
- Building footprints (*Cartosat-1*)   Building footprints (*Geoeye-1*)
- *Cartosat* DSM   *Geoeye* DSM   Buffer polygon
- Filtering DSM → Zonal statistics
- Validation with stereo measurements → Building height ($H_{median} - H_{minimum}$)
- Line of sight analysis ← Buildings draped over bare earth model

Figure 1 - Workflow of line of sight analysis using building footprints derived from the *Cartosat-1* and *Geoeye-1* datasets

The whole workflow was implemented within the 2015 version of the *Imagine* photogrammetry suite - an extension of *ERDAS IMAGINE* (*HEXAGON GEOSPATIAL*), and it was grouped into the six sub-stages for generating 3D point clouds, digital surface models and orthophotos, as shown in Figure 2.

In the first step, the images from *Cartosat-1* and *Geoeye-1* were imported as separate blocks. Image pyramids were generated from these images to reduce computation time and to increase the reliability of image-matching. In the second step, interior and exterior orientations were estimated for those *Cartosat-1* and *Geoeye-1* images that formed the block. Interior orientation defines the internal geometry of any sensor and image model and it is primarily used to transform the image pixel coordinate system into the image space coordinate system. Exterior orientation defines the position and angular orientation of the sensor that captured the image and it relates the sensor model via the distance between the image space and the ground space.

Cartosat-1 and *Geoeye-1* both provide rational polynomial coefficients (RPCs) with the images. These RPCs were used to define the initial functions for transforming the original sensor geometries into image geometries and for subsequent orientation of images relatively to each other. A good estimation of the exterior orientation was achieved. However, for subsequent pixel-based image matching the exterior orientation needs to be very precise and accurate (Perko et al., 2014). Therefore, the initial RPC functions were further refined using ground control points (GCPs) and tie points. Six GCPs were collected using geodetic class GPS receivers in differential mode with an observation period of one hour. The tie points were automatically computed through a multi-image, area-based correlation.
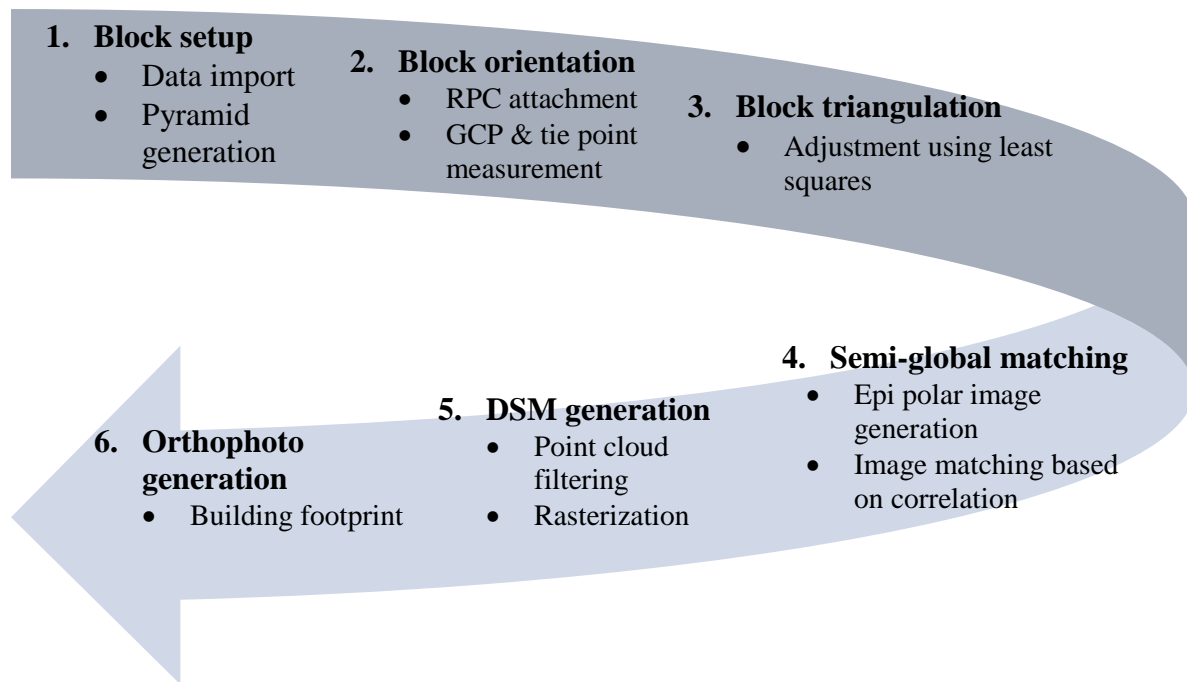
1. Block setup
- Data import
- Pyramid generation

2. Block orientation
- RPC attachment
- GCP & tie point measurement

3. Block triangulation
- Adjustment using least squares

4. Semi-global matching
- Epi polar image generation
- Image matching based on correlation

5. DSM generation
- Point cloud filtering
- Rasterization

6. Orthophoto generation
- Building footprint

Figure 2 - Photogrammetric workflow applied to high resolution stereo imagery for generating 3D point clouds, digital surface models and orthophoto generation

Finally, block triangulation was used to accurately tie together the images from separate blocks by using a least-squares adjustment in order to estimate the bundled solution for the entire block while minimizing and distributing the error. Accuracies achieved after block triangulation by *Cartosat-1* and *Geoeye-1* stereo pairs were 0.24 pixels and 0.12 pixels respectively.

3.1.1. Digital surface model generation using a semi-global matching technique

Our accurately triangulated images then served as input for semi global matching (Hirschmuller, 2008) to generate digital surface model information, and the semi global matching algorithm, which is in the *imagine* photogrammetry software, was developed by *Tridicon* was used to process satellite image pairs of *Cartosat-1* and *Geoeye-1* data.

Note that by applying energy minimization techniques within semi global matching using a smoothness constraint expressed as a global cost function, one can identify disparities whenever several line pairs intersect within one pixel simultaneously. More exactly, semi global matching computes conjugate points along multiple conjugate lines, pixel by pixel, and it does this hierarchically by using mutual information, instead of differences in intensity, as a dissimilarity measure.

In other words, our method's mutual information (MI) measured correspondence without assuming that conjugate points have similar intensity values, and such MI is robust because whenever it matches conjugate points it accounts for radiometric differences between images. But before the MI was computed we had to obtain an initial disparity image for warping one of the stereo images, and so a user-defined threshold was set for the disparity image pair in order to detect inconsistencies.

In this instance the initial disparity images for *Cartosat-1* and *Geoeye-1* were generated with rational polynomial coefficient thresholds of 0.5 pixels and 0.2 pixels respectively, and regularization was used to ensure a well-behaved reconstruction. This was because matching costs based on single pixel values or small windows are usually erroneous.

The matching step was in fact converted into an energy-minimization problem because the following discontinuity-preserving regularization was used.

$$E(D) = \sum_p (C(P, Dp) + \sum_{q \varepsilon Np} P1[|Dp - Dq| = 1] + \sum_{q \varepsilon Np} P2[|Dp - Dq| > 1] \qquad (1)$$

where:

> function C matches the cost for each pixel location, p, in the first image and the corresponding pixel in the other image, as defined by the disparity map D, and

> the second and third terms penalize disparity changes in the neighbourhood, Np, of each position p.

In other words, the penalty P1 is added for all disparity changes equal to one pixel, and if the disparity change is greater than 1 at larger discontinuities, a fixed cost P2 is added. That is, the function accounts for larger disparities between the neighbourhood pixels in areas of weak and high contrast.

Semi global matching was used to calculate the pixel-wise matching cost, or the dissimilarity between base-image pixel and match-image pixel, for all pixels located along the corresponding epi polar line in the match image (Hirschmuller et al., 2008). Matching cost was then aggregated from linear paths at every 45º from the possible match point. The minimum aggregated matching cost along the epi polar line was then used to calculate disparity and sub-pixel accuracy was achieved by fitting a local parabola to the aggregated costs around the minimum. Matching was done from the first to the second image and vice-versa, and only the consistent disparities were retained. Finally, semi global matching generated a dense, 3D, photogrammetric, point cloud with points at locations of consistent disparities.

Figures 3 and 4 respectively show the resulting digital surface modes (DSMs)for the study area based on the *Cartosat-1* and*Geoeye-1* datasets. That is, digital surface models in Lidar binary exchange format (LAS,) with resolutions of 10m and 2m respectively, were generated for the *Cartosat-1* and *Geoeye-1*datasets.
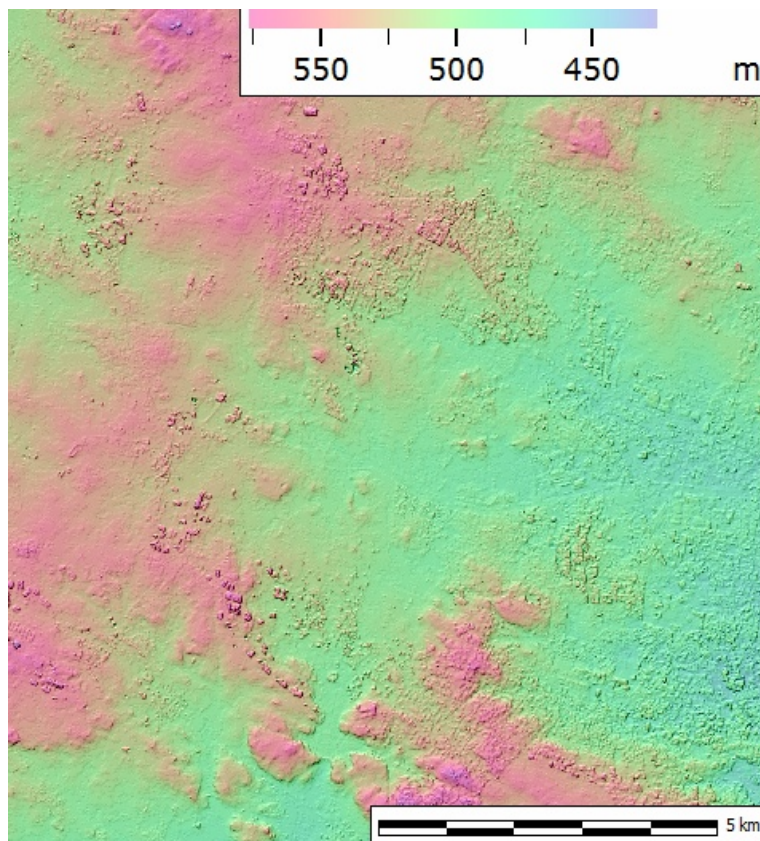
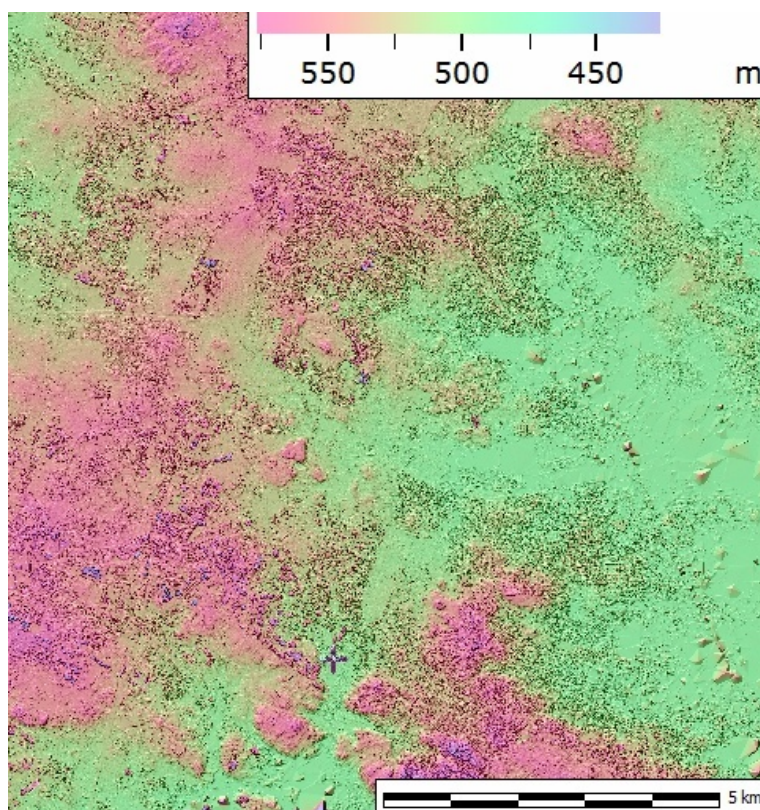**Figure 3 –** Digital Surface Model from the *Cartosat-1*dataset

Figure 4 – Digital Surface Model from the *Geoeye-1* dataset

3.1.2.   Orthophoto generation and manual vectorization in GIS

Block triangulation parameters, a digital surface model and the image which is nearest to nadir were then selected as inputs for the generation of orthophotos. Our orthophotos depicted the ground features in their true orthographic projection and we generated them using a cubic convolution, resampling method with output cell sizes of 2.5m and 0.5m respectively for the *Cartosat-1* and *Geoeye-1* data. Cubic convolution was chosen over other resampling methods because, since more cells are involved in the calculation of output values, it has a tendency to sharpen the edges of the data.

Note that in the first step, manual vectorization of building footprints was performed using *ArcGIS 10.3* software, and such manual vectorization has potential for achieving high accuracy levels. It also has the added advantage of demarcating the exact building shapes – something which is crucial in satellite visibility analysis.

The second step involved generation of buffered polygons using the proximity toolset within *ARCGIS 10.3* with reference to the existing building footprints. To compute lower-elevation buildings, buffer polygons of 25m for *Cartosat-1* and 20m for *Geoeye-1*were created around each individual building footprint so that the height values collected in the digital surface model were not influenced by building height. These buffer polygons included surrounding elevation data representing the ground or adjacent roads. Building footprints and buffered polygons were then assigned a unique identifier for further analysis.

3.2. Filtering the Digital Surface Model (DSM)

Since every photogrammetric point cloud contains outliers, filtering is needed to remove erroneous match points and, unsurprisingly, the raw surface models derived from semi global matching were generally polluted by artefacts, noise and outliers due to other errors. The latter included physical limitations of the image sensor, limited geometric accuracy of the model and matching errors due to occlusion, shadow and sun reflection (Tack et al., 2012). They result in differences in the DSM which are manifest as spikes and pits.

In order to address this problem we applied our classification technique to remove points that fell within the building footprints, or off the grid, using the *Terrascan* software. Its process of filtering (point cloud classification) reduces noise and errors within any surface model and it improves the building-block models.

The filtering algorithm used by *Terrascan* starts from a sparse Triangulated Irregular Network (TIN) and iteratively refines it towards the mass point set. At every iteration, points are added to the TIN if they are below data-derived thresholds in the form of critical distances from TIN facets and angles to the facet nodes (Axelsson, 2000). First, ground points are identified, and then large triangles are formed using those points. Since the terrain slope is usually different from the slope seen between the ground and the tops of trees and buildings, slope difference is used to separate ground and non-ground points.

3.3. Deriving building height

Zonal statistics were used to derive correct building heights from point cloud data. Specifically, average, median (50th percentile), lower quartile (25th percentile) and upper quartile (75th percentile) were calculated within the building footprint and they were verified using reference heights derived manually from stereoscopic parallaxes of roofs and bases of buildings in a stereo model. This approach aimed to select the statistical height, which is the best approximation of correct building height.

Evaluation was carried out using descriptive statistical parameters such as Standard Deviation, Mean Absolute Error (MAE) and Root Mean Square Error (RMSE). Standard Deviation describes the spread of differences in height with reference to the mean. Mean Absolute Error describes the average error magnitude of the differences in height without

considering their direction and it is linear, which means that all of the individual differences are weighed equally in the average. Root Mean Square Error is a quadratic scoring rule that measures the average magnitude of the error.

Using *ARCGIS 10.3*, the building footprints with unique identifiers were linked to both elevation, as derived from the bare earth digital elevation model, and roof height elevation. This enabled us to extract the buildings in 3D. The latter were then draped onto the bare earth digital elevation model for line of sight analysis with GPS satellites.

3.4. Line of sight analysis with GPS satellites and GIS Implementation

Once the building heights were derived and applied to the building footprints, line of sight analysis with the observer position and target location was carried out using *ARCGIS 10.3*. The latter's line of sight tool requires specification of two points on a line, the first and last vertex. One point is the observer and the other is the target. Later, visibility is calculated through the ray tracing method.

In this study, the observer position was selected 2.5m above ground level and the target locations were kept at actual elevations and azimuths of satellites. To perform line of sight analysis for GPS satellites, the elevation angle and the azimuth for each satellite to a specified point on the earth's surface was considered. The elevation angle ranged from 0º to 90º and it was measured from a plane, tangential to the ground, to the point directly above the observer (90º). The azimuth was the compass direction of the spacecraft, measured clockwise from north and ranging from 0º to 360º.

Line of sight was carried out by generating sight lines at actual elevation and azimuths of GPS satellites. To predict the satellite positions several techniques, like those employing a two-line element set (33) or the keplerian elements used in the *GRASS* module (35) were available. These techniques are complex in terms of user training and are heavy in terms of computational performance.

So to avoid these limitations, a freely available GNSS prediction software from *Trimble Planning* was used to predict the pseudo satellite locations, thereby minimizing cost and time. The output gave information about the azimuth and elevation to each satellite from a known observer point, and using this information to calculate pseudo satellite positions enabled us to avoid the need for a coordinate transformation from the earth-centred system to the Universal Transverse Mercator system (UTM). To ensure the simulated satellites was not too close to the survey site which would mean that they would have magnified the field of view. They were simulated at a distance of 15 km from the observer's position.

For the initial tests, a particular day and time for conducting the test was selected for the *Cartosat-1* area (10.00 A.M) and the *Geoeye-1* area (11.00 A.M). A single point (observer location) at a specified latitude, longitude and time was chosen to perform line of sight analysis, using true elevation and azimuth data, with GPS satellites. The elevation and azimuth of the GPS satellite in this study area were derived from the *Trimble Planning* software at a specified latitude, longitude (observer location) and time. The output was exported to HTML format and then evaluated using an HTML editor. The positions of GPS satellites were in a spherical coordinate system, as shown in Figure 5.
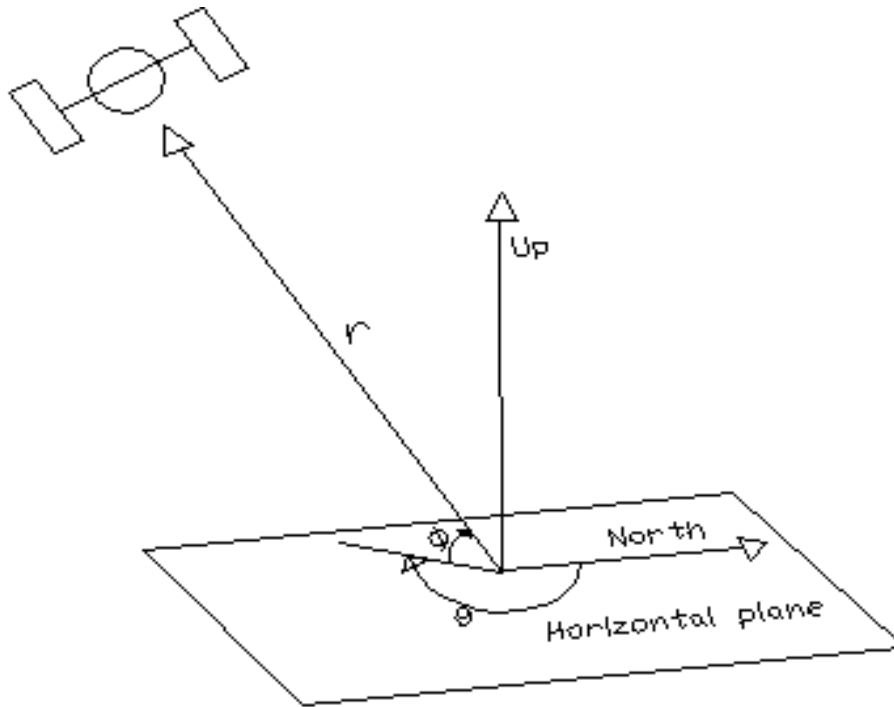
Figure 5 - Angles of azimuth and elevation from GPS satellite

To carry out the coordinate transformation open source 'R', as developed by the R Core Team (2013) was used. Conversion used the geometric formulae shown in equations 2, 3 and 4 to transform coordinates X, Y and Z respectively to their pseudo positions X', Y' and Z'. This was done using the *Trimble Planning* software's values of 15km for simulated range along with its estimates for the measured azimuth and elevation.

$$X' = r*cos(\emptyset)*cos(\theta) \tag{2}$$
$$Y' = r*cos(\emptyset)*sin(\theta) \tag{3}$$
$$Z' = r*sin(\emptyset) \tag{4}$$

where:

r is the range,

$\emptyset$ is the elevation measured from x-y plane, and

θ is the azimuth from x axis.

For inter visibility analysis between the observer and the target, sightlines need to be generated as shown in Figure 6. Inter visibility analysis was carried out to determine the visibility of sight lines through potential obstructions. which can be a combination of raster multi patches, Triangulated Irregular Networks (TINs) and extruded polygons. In this study, building footprints, which were extruded using the height attribute, were regarded as being potential obstructions.
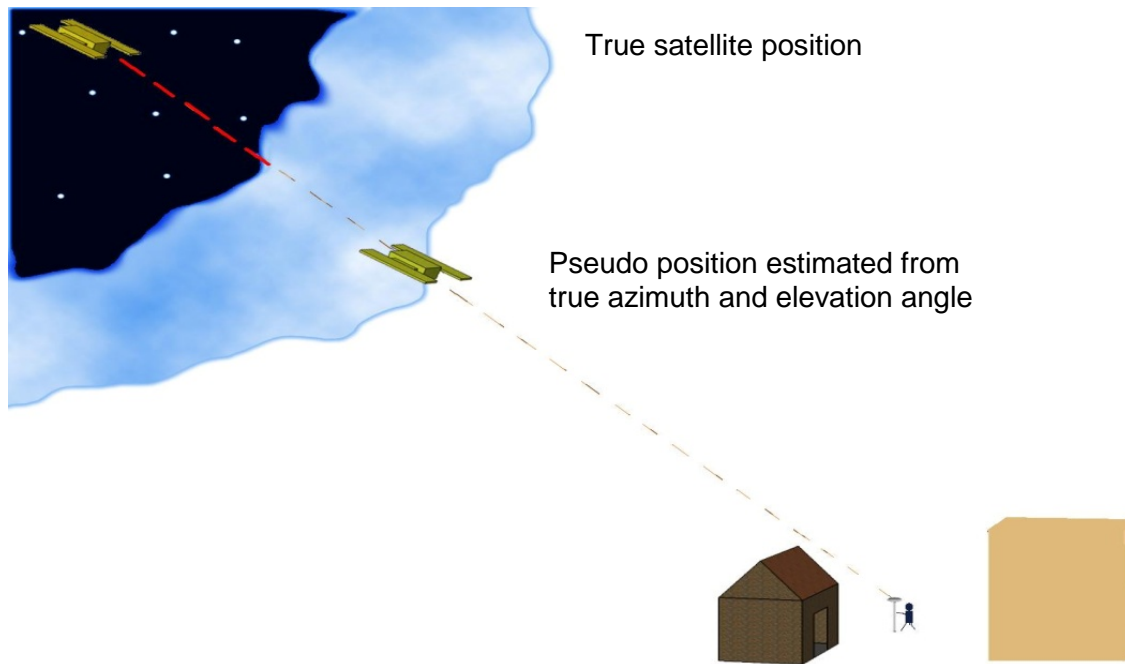
True satellite position

Pseudo position estimated from
true azimuth and elevation angle

Figure 6 - Creating a sightline from observer to pseudo satellite position

4. Results and discussion

In the case of the *Geoeye-1* data, higher spatial (0.41m) and spectral resolution (11bits) improved the feature capturing of buildings with a minimum loss of information. Indeed, many of the buildings were captured as individual buildings along with detailed building extensions (Figure 7). For the *Cartosat-1* data, coarser spatial resolution (2.5m) meant that the buildings were generalized into groups of buildings in dense urban areas (Figure 8). Moreover, the DSM from *Geoeye-1* was well represented in dense urban areas as fine structures and the boundaries of buildings were clear. The number of satellites available was ten at 10.00 am and nine at 11.00 am, and the elevation cut off angle was 10 degrees for both the *Cartosat-1* and *Geoeye-1* areas.

Figure 7 - Building footprints from *Geoeye-1*

Figure 8 - Building footprints from *Cartosat-1*

However, each dataset has its own merits. For instance, whereas *Geoeye-1* data is superior in terms of spatial and spectral resolution, *Cartosat-1* data's fixed view angles during imaging ensures uniform accuracy over a single image as well as over images taken from different orbits. Also, compared to *Geoeye-1* data the wider swath of *Cartosat-1* results in fewer scenes being needed to cover the same area.

Building heights were derived from the respective digital surface models and they were validated with stereo measurements used as reference heights. The latter were of much higher quality than those taken from the automatically generated digital surface model. The differences between statistically derived roof height and reference height were summarized using three descriptive parameters, as shown in Table 2. Clearly, the median height parameter gives the best approximation of building height when compared with reference height for the *Cartosat-1* and *Geoeye-1* datasets. That is, based on descriptive statistics, the best approximation of building heights was achieved when building footprints were used to derive urban 3D models.

Cartosat-1 cf *Geoeye-1*			
	Average height	**First-quartile height**	**Median height**
Standard Deviation (m)	1.35 cf 1.63	1.67 cf 1.51	1.46 cf 1.99
Mean Absolute Error (m)	3.75 cf 2.98	4.73 cf 3.87	3.57 cf 1.96
Root Mean Square Error(m)	4.14 cf 3.33	5.18 cf 4.14	3.73 cf 2.30

Table 2 - Comparing *Cartosat-1* and *Geoeye-1*

Figures 9 and 10 show the box-and-whisker plots of differences between reference data building heights with statistically derived building heights (q1h, average, median and q3h) for Cartosat-1 and Geoeye-1 areas. The solid line inside the box is the median; boxes cover the interquartile range and whiskers extend outwards from the boxes to 1.5 times the interquartile range.
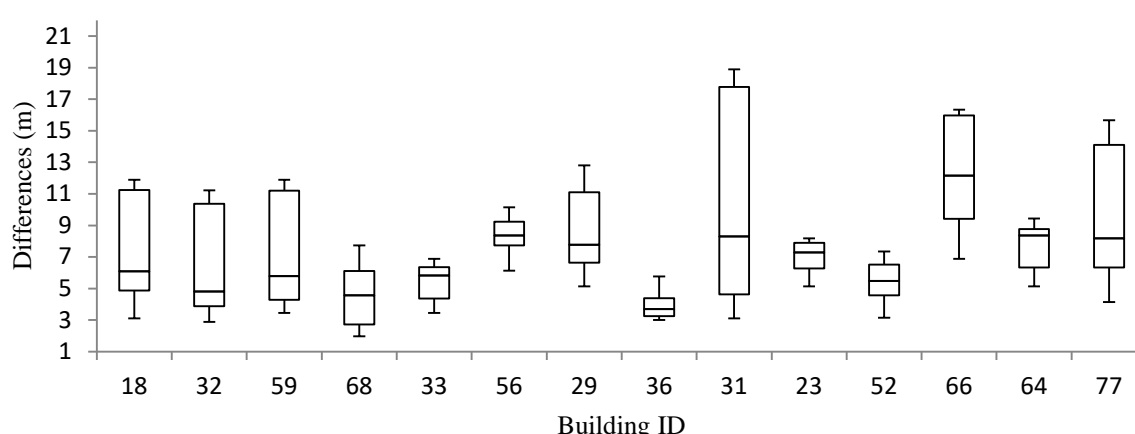

Figure 9 - Box–and-whisker plot representing the differences between first-quartile, median, average and third-quartile building heights and reference heights using the *Cartosat-1* data.
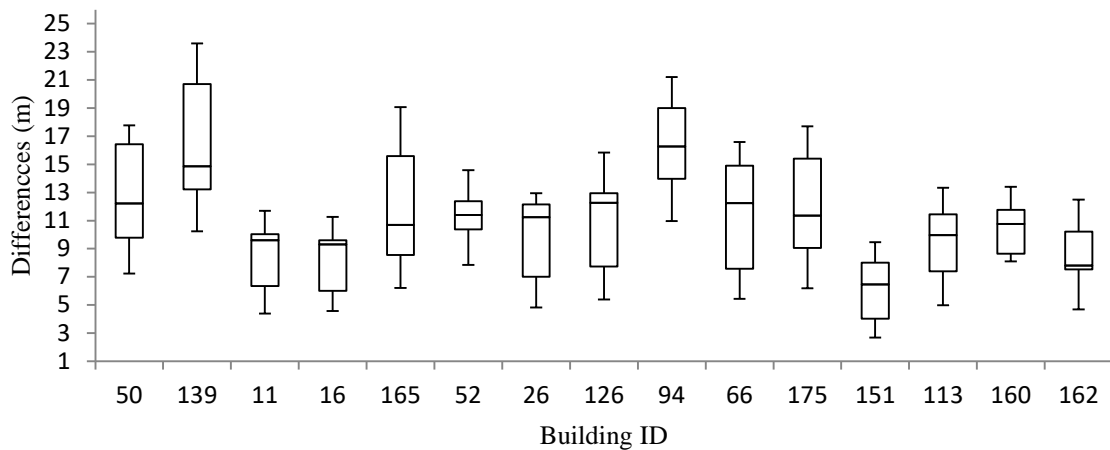
Figure 10 - Box–and-whisker plot representing the differences between first-quartile, median, average and third-quartile building heights and reference heights using the*Geoeye-1*data.

Figures11and12 show the lines of sight between the visible satellites and the GPS receiver. Green lines show the satellites which were visible, and the red ones show those which were obstructed due to buildings. The GPS location was in a wide road and in a narrow lane.

In the*Cartosat-1* area there were four visible satellites; three had an elevation angle of more than 30 degrees and one had an elevation angle of 12 degrees. Nevertheless, the fourth satellite was visible because there was no potential obstruction from buildings at that particular azimuth of the GPS' satellite.

In the *Geoeye-1* area there were two visible satellites, both with an elevation angle of more than 15 degrees, and there were no potential obstructions from buildings at that particular azimuth of GPS' satellite. But since urban sprawl was less marked in 2005 compared to 2012, buildings were fewer and this, combined with the higher elevation angles of the GPS' satellites meant that the number of visible satellites was higher for*Cartosat-1*than for *Geoeye-1*.
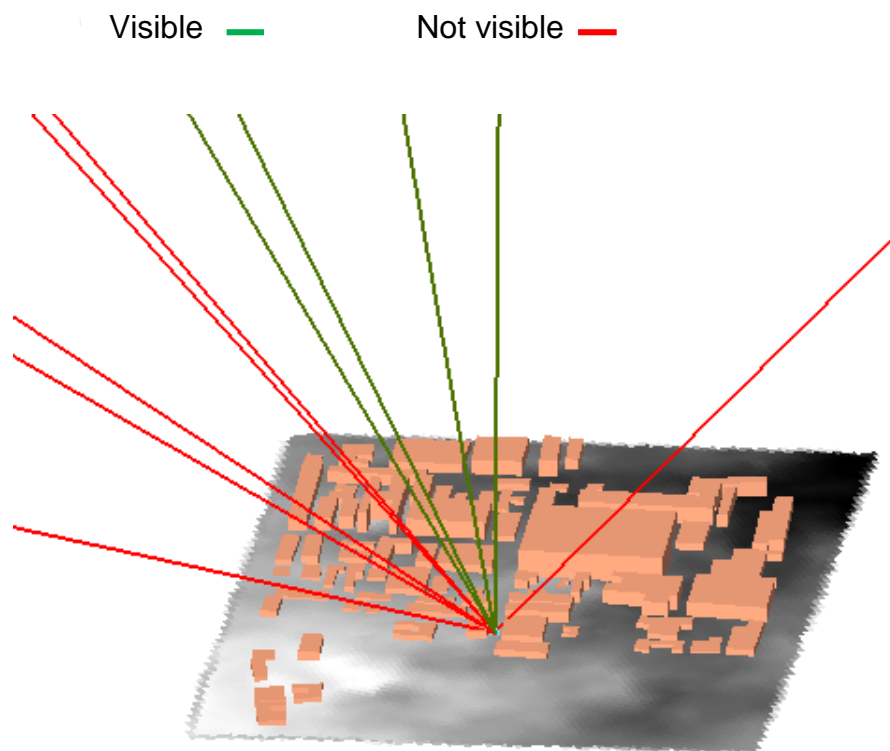
15

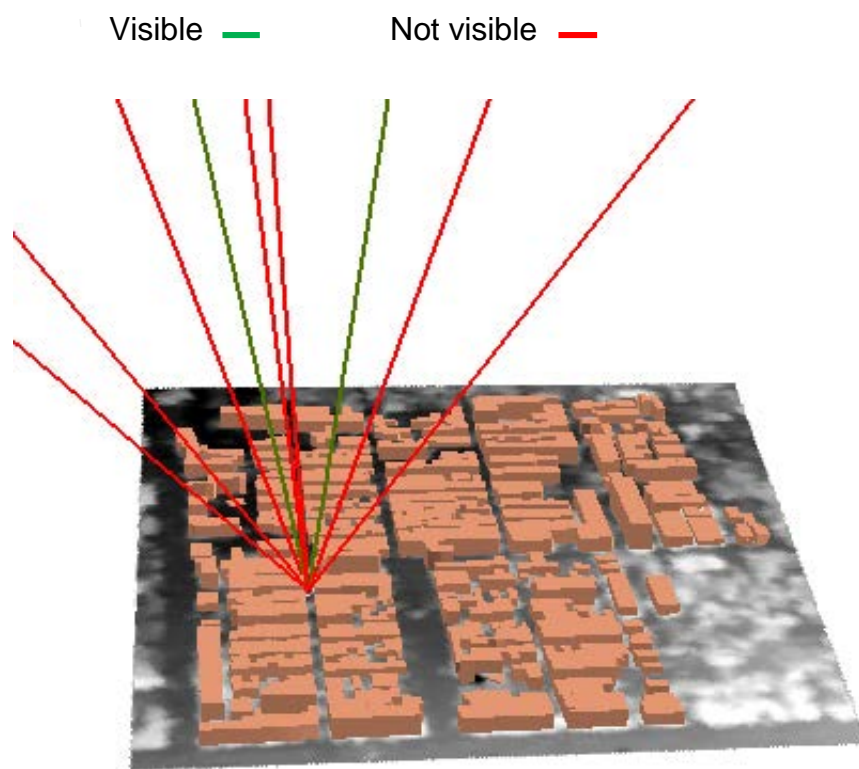**Figure11 -**Line of sight analysis with visible satellites from *Cartosat-1*

Figure 12 -Line of sight analysis with visible satellites from *Geoeye-1*

5. Conclusions

This study has developed a novel approach that combines freely available Global Navigation Satellite System (GNSS) prediction software, GIS, two-dimensional vectors captured from orthoimages and elevation data derived from high-resolution digital surface models that predict satellite visibility. It helps to avoid having to undertake time-consuming, laborious and costly high-density, topographic surveys using electronic levelling instruments.

Our methodology can easily be applied to existing two-dimensional vectors, combined with basic elevation data, to carry out line of sight analysis with GPS satellites. It can also facilitate identification of complex areas prior to any mobile survey because it helps GNSSs address signal blockage and reflection problems caused by tall buildings within urban areas. Moreover, it can do this in real-time using GPS satellites and algorithms for GPS solving signal obstruction problems in a more practical way.

In summary, our work has overcome some limitations of traditional, mission-planning software for GPS receivers. It effectively combines high-resolution satellite imagery, manual vectorization and advanced, dense image-matching techniques at low run-time for line of sight analysis when using GPS satellites. We have shown how high-resolution satellite data, building footprints and digital surface models can generate urban 3D models that exhibit a Root Mean Square Error of only 3.7m (*Cartosat-1*) and 2.3m (*Geoeye-1*). Such models can be a valuable input to readily available, GNSS prediction software within dense urban areas and they can be combined seamlessly with GPS data for real-time, mobile applications like road transport, fleet and asset tracking, traffic management, security and surveillance.

In the *Geoeye-1* study area our receiver was unable to track the required minimum number of satellites due to the density of urban development, but this can be successfully addressed by integrating GPS with other positioning systems and sensors, such as accelerometers, gyroscopes, odometers speedometers and dopplometers, or by using complementary technologies like cellular networks. Direct line of sight to visible satellites can be achieved by incorporating almanacs from freely available GNSS prediction software.

There is scope for further work in the form of using multipath signals from GPS satellites in dense urban areas. Since the Indian Space Research Organization (ISRO), has embarked upon two satellite-navigation programs - GPS Aided Geo Augmented Navigation (GAGAN) and the Indian Regional Navigation Satellite System (IRNSS) the potential of these methodologies with mobile applications is particularly high. Our methodology will augment mission-planning software for better real-time, urban mobile applications.

Acknowledgements

References

Axelsson, P. (2000) - DEM generation from laser scanner data using adaptive TIN models. *IAPRS*, 33. Part B4/1,110-117.

Briese C. & Pfeifer N. (2001) - Airborne laser scanning and derivation of digital terrain models. *Proceedings of the 5th Conference on Optical 3D Measurement Techniques*, Austria, 80-87.

Cahalane, Conor (2015) - Combining 2D Mapping and Low Density Elevation Data in a GIS for GNSS Shadow Prediction, *ISPRS International Journal of Geoinformation*, 4, 2769-2791.

Deepika Kumara & Kamaljit Kaur (2016) - A survey on stereo matching techniquesfor3D vision in image processing, *International Journal of Engineering and Manufacturing*,4, 40- 49, http://www.mecs-press.net/ijem (accessed on March 28, 2017).

Fraser, C.S. & Ravanbakhsh, M. (2009) - Georeferencing accuracy of GeoEye-1imagery, *Photogrammetry Engineering and Remote Sensing*, 75 (6), 634–638.

George Taylor, Jing Li, David Kidner, Chris Brunsdon & Mark Ware (2007) – Modelling and prediction of GPS availability with digital photogrammetry and LiDAR, *International Journal of Geographical Information Science*, 21 (1), 1-20.

Grodecki, J. & Dial, G. (2003) - Block adjustment of high-resolution satellite images described by rational polynomials, *Photogrammetry Engineering and Remote Sensing*, 69 (1), 59–68.

Grewal, M.S., Weill L.R. & Andrews, P.A. (2007) - Fundamentals of satellite and inertial navigation, in *Global Positioning Systems, Inertial Navigation and Integration*, 2nd ed; Wiley: Interscience, NJ, USA, 34–48.

Groves, P., Jiang, Z., Wang, L. & Ziebart, M. (2012) - Intelligent urban positioning, shadow matching and non-line-of-sight signal detection, *Satellite Navigation Technologies and European Workshop on GNSS Signals and Signal Processing (NAVITEC), 6th ESA Workshop*, December, 1–8.

Guth, P.L. (2004) - The geometry of line-of-sight and weapons fan algorithms, in Caldwell D.R, Ehlen J, Harmon RS (eds) - *Studies in military geography and geology*, Kluwer Academic, Dordrecht, chapter 21, 348 pages.

Haala, N. & Kada, M. (2010) - An update on automatic 3D building reconstruction, *ISPRS Journal of Photogrammetry and Remote Sensing*, 56, 570–580.

Hirschmüller, H. & Scharstein, D. (2007) - Evaluation of Cost Functions for Stereo matching. Computer Vision and Pattern Recognition. *IEEE Conference*, 1–8.

Hirschmueller, H. (2008) - Stereo processing by semi-global matching and mutual information, *IEEE Transactions on Pattern Analysis and Machine Intelligence*, 30 (2), 28-41.

Mesev, V. (2003) - Remotely sensed cities: an introduction, in Mesev, V. (Ed.) - *Remotely Sensed Cities*, Taylor and Francis, London, 1–20.

Mitchell, G. & MacNabb, K. (2010) - High resolution stereo satellite elevation mapping accuracy assessment, *Proceedings of the Annual ASPRS Conference,* 1–12.

Mohsen Ghanea., Payman Moallem & Mehdi Momeni (2016) - Building extraction from high-resolution satellite images in urban areas: recent methods and strategies against significant challenges, *International Journal of Remote Sensing*, 37 (21), 5234-5248.

Muralikrishnan, S., Abhijit Pillai., Narender, B., Shashivardhan Reddy., Raghu Venkataraman & Dadhwal. V.K. (2012) - Validation of Indian National DEM from Cartosat-1 Data, *Journal of the Indian Society of Remote Sensing*, online 28 March 2012.

Nalpantidis, L. & Sirakaulis, G.Ch. (2007) - Review of stereo algorithms on 3D vision, *Sixteenth International Symposium on Measurement and Control in Robotics*, 116-124.

Nandakumar, R., Amitabh., Chamy, M. P.T., Kopparthi, S.S.S., Paswan, G., Prakash, S. & Singh, S. (2008) - Synthesis of investigations under ISPRS-ISRO Cartosat-1 scientific assessment programme primarily for DSM generation. *ISPRS International Archives of the Photogrammetry, Remote Sensing and Spatial Information Sciences*, XXXVII (Part B1), 1279-85.

Partovi, T., Huang, H., Krauss, T., Mayer, H. & Reinartz, P. (2015) - Statistical building roof reconstruction from World View-2 stereo imagery, *ISPRS International Archives of Photogrammetry Remote Sensing & Spatial Information Sciences*, XL-3/W2, 161–167.

Perko, R., Raggam, H., Gutjahr, K. & Schardt, M. (2014) - Assessment of the mapping potential of Pléiades stereo and triplet data, *ISPRS International Archives of the Photogrammetry, Remote Sensing & Spatial Information Sciences*, 2 (3), 103- 109.

Poon, J., Fraser, C., Chunsun, Z. & Li, Z., (2005) - Quality assessment of digital surface models generated from IKONOS imagery, T*he Photogrammetric Record,* 20 (110), 162–171.

R Core Team (2013) - *R: A language and environment for statistical computing,* R Foundation for Statistical Computing, Vienna, Austria. URL http://www.R-project.org/.

Sohn, G., Huang, X. & Tao, V. (2008) - A data-driven method for modelling 3D building objects using a binary space partitioning tree, in J. Shan & C. K. Toth (Eds.) - *Topographic Laser Ranging and Scanning: Principles and Processing*, Boca Raton, CRC Press, 479 – 50.

Scharstein, D. & Szeliski, R. (2002) - A taxonomy and evaluation of dense two-frame stereo correspondence algorithms, *International Journal of Computer Vision*, 47(1/2/3), 7-42.

Sreedhar, M., Muralikrishnan, S. & Dadhwal, V.K. (2015) - Automatic Conversion of DSM to DTM by Classification Techniques Using Multi-date Stereo Data from Cartosat-1, *Journal of the Indian Society of Remote Sensing*, 43, Online 18 February, 2015.

Sithole, G. & Vosselman, G. (2004) - Experimental comparison of filter algorithms for bare-earth extraction from airborne laser scanning point clouds, *ISPRS Journal of Photogrammetry and Remote Sensing*, 59 (1-2), 85–101.

Tack, F., Buyuksalih, G. & Goossens, R. (2012) - 3D building reconstruction based on given ground plan information and surface models extracted from spaceborne imagery, *ISPRS Journal of Photogrammetry and Remote Sensing*,67, 52–64.

Toutin, T. (2001) - Elevation modelling from satellite visible and infrared (VIR) data: a review, *International Journal of Remote Sensing*, 22 (6), 1097–1225.

Toutin, T. (2004) - Comparison of stereo-extracted DTM from different high resolution sensors: SPOT-5, EROS-a, IKONOS-II, and QuickBird, *IEEE Transactions on Geoscience and Remote Sensing*, 42 (10), 2121–29.

Trimble Planning (2015) - Desktop software, http://www.trimble.com/planningsoftware_ts.asp (accessed on 12 December 2016).

Zhang, K.S., Chen, D., Whitman, M., Shyu, J. Yan & Zhang, C - (2003) - A progressive morphological filter for removing nonground measurements from airborne LIDAR data, *IEEE Transactions on Geoscience and Remote Sensing*, 41(4), 872-882.

Zhang, L. (2005) - Automatic digital surface model (DSM) generation from linear array images, PhD Dissertation 88, *Institute of Geodesy and Photogrammetry*, ETH Zurich, Switzerland, 199 pages.